applied sciences

MDPI

Article

The Thermal Resistance Performance of WTi Alloy-Thin-Film Temperature Sensors Prepared by Magnetron Sputtering

Zhengtao Wu [1,2], Yintuan Zhang [1], Qimin Wang [1,*], Kwang-Ho Kim [3] and Se-Hun Kwon [3]

[1] School of Electromechanical Engineering, Guangdong University of Technology, Guangzhou 510006, China; ztwu@gdut.edu.cn (Z.W.)
[2] Guangdong Provincial Key Laboratory of Advanced Manufacturing Technology for Marine Energy Facilities, Guangdong University of Technology, Guangzhou 510006, China
[3] School of Materials Science and Engineering, Pusan National University, Busan 609-735, Republic of Korea
* Correspondence: qmwang@gdut.edu.cn

Abstract: The microstructure and properties of WTi alloy films with 0~23 at.% Ti prepared by magnetron sputtering were investigated. The electrical resistivity gradually increased with the increase in the Ti content. When the Ti content was 6.8 at.%, the temperature coefficient of resistance of the alloy film reached the maximum value of 19.5×10^{-4} K^{-1}, which is 3.6 times higher than that of the pure W film. After several thermal resistance tests, the temperature coefficient of resistance of the WTi alloy film with 6.8 at.% Ti decreased gradually. After five measurements, the temperature coefficient of resistance decreased gradually from 19.5×10^{-4} to 16.3×10^{-4} K^{-1}. After annealing at 500 °C for 30 min, the grain size of the WTi alloy film (6.8 at.% Ti) increased, a few pores appeared, and the density of the film decreased. The temperature coefficient of resistance decreased from 19.5×10^{-4} K^{-1} to 14×10^{-4} K^{-1}. When the annealing time was increased to 60 min, the structure and properties of the WTi alloy film remained basically unchanged. After conducting the annealing treatment for 30 min, the WTi films showed excellent stability in the thermal resistance tests, and their temperature coefficient of resistance was basically consistent after cyclic thermal loading, which has promising application prospects for the temperature measurement of tools and dies.

Keywords: magnetron sputtering; thermal resistance film; WTi alloy film

check for updates

Citation: Wu, Z.; Zhang, Y.; Wang, Q.; Kim, K.-H.; Kwon, S.-H. The Thermal Resistance Performance of WTi Alloy-Thin-Film Temperature Sensors Prepared by Magnetron Sputtering. *Appl. Sci.* **2023**, *13*, 4747. https://doi.org/10.3390/app13084747

Received: 15 March 2023
Revised: 23 March 2023
Accepted: 7 April 2023
Published: 10 April 2023

1. Introduction

In the energy, petrochemical, and aerospace industries, a large number of components work in high-temperature environments and in fatigue loading. Stress corrosion under complex conditions places high demands on the performance of the material, making the analysis of the material in high-temperature failure mechanisms very important. However, the first step in the analysis of high-temperature failure is the real-time detection of temperature. Especially in the tool and die, the real-time detection of the temperature in the working process can determine the high-temperature failure of materials, calculate their service life, and design the corresponding cutting parameters for different materials in the cutting tool. Therefore, the real-time detection of the temperature can not only provide a reliable basis for the design and preparation of high-temperature-resistant materials but also adjust the working parameters through the change in temperature so as to prolong their service life. Most sensors are discrete devices and cannot be installed on the surface of the parts to measure temperature and, therefore, the temperature sensor in the cutting tool has a very limited ability to detect temperature.

Thin-film temperature sensors have a small size and a thickness of a micron; so, the heat capacity of thin-film temperature sensors is small and their response to temperature changes is rapid [1,2]. Because the thin film sensor is directly deposited on the workpiece to be measured, it is closer to the point to be measured than discrete sensors and can better reflect the temperature of the point to be measured [3–5]. Additionally, because

the thin-film temperature sensor area is small and the sensor is thin, it can be used in small spaces and to ensure the assembly precision of high-temperature measurements [6–8]. Thin-film thermal resistance can be divided into semiconductor thermistors and metal thermistors according to their different materials. The reported thermistors are shown in Table 1, including the deposition techniques and temperature coefficient of resistance (TCR) values.

Table 1. Research status of thermal resistance.

Materials	Deposition Technique	Temperature [°C]	TCR [$\times 10^{-4}$ K^{-1}]	Refs
Pt	RF magnetron sputtering	-	38.5	[9]
Ti/Pt	Sputtering	−70~600	22.7	[10]
Pt	/	25~90	22.18	[11]
Pt	Electro-magneto sputtering	20~540	39	[12]
Ni	dc magnetron sputtering	20~120	63	[13]
Ni	Screen printing	0~200	30	[14]
Ni	dc magnetron sputtering	25~200	30	[15]
Ni	dc magnetron sputtering	0~400	50	[16]
Ti	Arc ion plating	-	19.7	[17]
Al	Magnetron sputtering	-	17.14	[17]
Al	dc magnetron sputtering	0~140	43.3	[18]
Al	Thermal evaporation	25~31	37.9	[19]
Cu	Thermal evaporation	25~31	38.2	[19]
Au	Thermal evaporation	25~31	33.5	[19]
Pd	dc magnetron sputtering	−180~230	15	[20]
Ni-Cr	RF magnetron co-sputtering	25~95	30	[21]
Ni-Cu	Magnetron sputtering	20~260	~56	[22]
Ti-W	dc magnetron sputtering	25~100	20	[23]
Cu_2O	Femtosecond laser reduction patterning	20~70	−55	[24]
$V_{1.85}W_{0.15}O_5$	RF magnetron sputtering	0~700	34.5	[25]
W/WO_3	dc magnetron sputtering	0~200	8.16	[26]
ITO	RF sputtering	0~900	21.51	[27]
Ni-ZrO_2	Metallo-organic deposition	20~300	~36.6	[28]
Silicon	PECVD	−40~125	16.25	[29]
Carbon Nanotube	CVD	22~200	10.3	[30]

Common semiconductor thermistors are oxides or compounds of metals and parts of semiconductor metals. Mizoshiri [24] used the femtosecond laser reduction method to fabricate a Cu_2O-rich nano-particle micro temperature sensor, which consisted of a Cu_2O-rich sensing part and a Cu-rich electrode. The resistance temperature coefficient of the prepared micro-temperature sensor is -55×10^{-4} K^{-1}, and the resistance characteristic of this negative value is consistent with the resistance characteristic of the Cu_2O semiconductor. The $V_{1.85}W_{0.15}O_5$ thin films prepared by the RF sputtering method by Nam have good TCR and dielectric properties [25]. It was found that the crystallization and thermoelectric properties of V1.85W0.15O5 films at different annealing temperatures are closely related to the grain size. After annealing at 400 °C, the dielectric constant of the $V_{1.85}W_{0.15}O_5$ film was 44, the dielectric loss was 0.83%, and the TCR value was about 34.5×10^{-4} K^{-1}. Sundeen [28] deposited cermet films with better thermal sensitivity than Pt and Ni films on Si substrates, with TCR values up to 42×10^{-4} K^{-1}. The superior sensor performance makes the design of Ni-ZrO_2 cermet resistors have advantages in thermal and flow sensor applications in terms of size and sensitivity. Mehmood [29] prepared p-type silicon thermal resistors and evaluated their power consumption, linearity, hysteresis, repeatability, reproducibility, and life expectancy. The p-type silicon thermal resistor has a very low power consumption (only 0.9 μW) and a sensitivity of 13.88 Ω/K, which is much higher than the Pt thermal resistor reported previously. Moreover, the thermal resistance of p-type silicon has a good linear response (98.9%), good repeatability, and significant low hysteresis, with a maximum variation of 0.2% between positive and negative cycles.

The temperature measurement mechanism of metal thermal-resistant films is that the vibration of metal atoms increases with the rise in temperature, and the scattering of electrons by lattice increases, leading to the increase in metal resistance. Therefore, the change in temperature can be reacted according to the change in resistance. Schmidl [10] introduced the effects of sputtering power and pressure on the growth, morphology, and electrical properties of the microstructure of Pt thin films. Pt thin films grow in columns at a high Ar pressure with a rough surface, contrary to thin films deposited at 0.5 Pa. It was shown that the increase in pressure and the decrease in power lead to a higher conductivity and higher temperature resistivity (TCR). In addition, the effects of two different substrate materials, thermal silicon oxide, and Al_2O_3 ceramic on the electrical properties and the growth of crystalline films were also discussed. The Pt film deposited on the Si substrate showed a (100) orientation, while the Pt film deposited on the Al_2O_3 substrate grew preferentially with the (111) peak. It is often noted that the sensitivity of thin films deteriorates as the device size decreases compared with that of single-crystal thin films. To overcome this problem, Wada studied the relationship between the deposition temperature and crystal structure in depth. Pt thin films with a thickness of 400 nm were prepared by magnetron sputtering on a sapphire single-crystal substrate (0001) and heated from 300 °C to 540 °C. Wada [12] found that the matrix temperature plays a key role in obtaining a high TCR, and the optimal value of the TCR obtained at 540 °C was 39×10^{-4} K^{-1}, while the high bonding strength and low surface roughness were maintained. Cui [15] used the DC magnetron sputtering method to prepare thermal-resistant nickel films at a low temperature. The results showed that compact and uniform nickel films can be prepared at room temperature. The thermal resistance coefficient of the Ni thin film prepared at room temperature was about 30×10^{-4} K^{-1} and had good repeatability at a circulating temperature. Stankevi [18] proposed using aluminum film resistors as temperature sensors to compensate for the output of heat sensitivity and bias displacement pressure sensors. In order to optimize the process parameters of this kind of temperature resistance, Al films with different thicknesses and heat treatments were studied experimentally. The results showed that the Al films with a thickness of 1.2 μm have good long-term stability after annealing at 330 °C for 72 h. The specific resistance is 2.85 μΩ·cm, and the resistance temperature coefficient is 43.3×10^{-4} K^{-1}. Oliva [19] studied the resistance temperature coefficients of Au and Al films with thicknesses ranging from 20 nm to 200 nm at 298 K and atmospheric pressure. The measured TCR value decreased with the decrease in film thickness, and the value decreased by about 13% compared with the corresponding volume value. Using cylindrical PET monofilaments as the main substrate, Eom [21] used RF magnetron co-sputtering to deposit unpatterned Ni–Cr films. By changing the sputtering power of the target material, Ni–Cr thermal-resistant films with different Cr contents were obtained. The higher the Cr concentration, the longer the diameter and height of the grain, and the more obvious the effect. In addition, the increase in Cr concentration worsened the crystallinity of the NiCr films, becoming closer to the amorphous phase. The TCR of different NiCr concentration ratios showed different characteristics, and the maximum TCR value was 30×10^{-4} K^{-1}.

Tungsten films have potential applications in temperature sensors due to their low cost, good conductivity, and stable physical/chemical properties [26]. However, their TCR values are relatively lower than that of typical industrial Pt resistance thermometers (~3.85×10^{-3} K^{-1} [31,32]). Thin-film Pt has the advantages of a high temperature coefficient of resistance, small volume, small heat capacity, and low thermal noise, which make it the focus of scientific research and industrialization. The TCR is a key technical index to characterize resistance thermometers' performance. The key factors affecting TCR value include film thickness, substrate roughness, and thermal annealing treatment. Interface scattering, annealing-induced grain growth, and defect reduction have a significant impact on TCR values [33–36]. Therefore, the purpose of this work is to alloy Ti into W to fabricate solid-solution-type WTi alloy films. The alloying helps decreases the melting point of the

alloys and thus the sputtered alloy films have a larger grain size. In addition, annealing was applied to improve the TCR values and stability of the WTi resistance thermometers.

2. Experimental Procedures

We used a vacuum ion-coating machine in the pretreatment of the p-type doped conductive silicon wafer (resistivity 5×10^{-4} Ω·cm) and quartz wafer (resistivity >100 MΩ·cm). WTi alloy films and ~600 nm thick W were deposited. In the deposition process, Ar (99.99%) was passed in the chamber as sputtering gas. The target material used for the deposition of W film was $470 \times 110 \times 8$ mm^3 pure W target, and the target material used for the deposition of WTi alloy film was W and Ti splice targets of the same size, and their schematic diagram is shown in Figure 1a. In the sputtering process, there are fewer Ti atoms near the upper end of the splicing target, but more Ti atoms near the lower end of the splicing target. Therefore, by changing the clamping position of the matrix, WTi alloy films with different Ti contents can be obtained. The specific deposition parameters are shown in Table 2. Figure 1b shows an image of a stainless-steel mask used for the WTi film deposition. The mask size was 30×30 mm^2. Figure 1c shows an image of the patterned WTi alloy film sensor. The line width was ~200 μm. The W and WTi alloy film thicknesses were kept at 591~664 nm (Table 2) to minimize the impact of thickness on film resistivity. The initial film resistance at RT was in the range of 55.8~73.8 Ω.

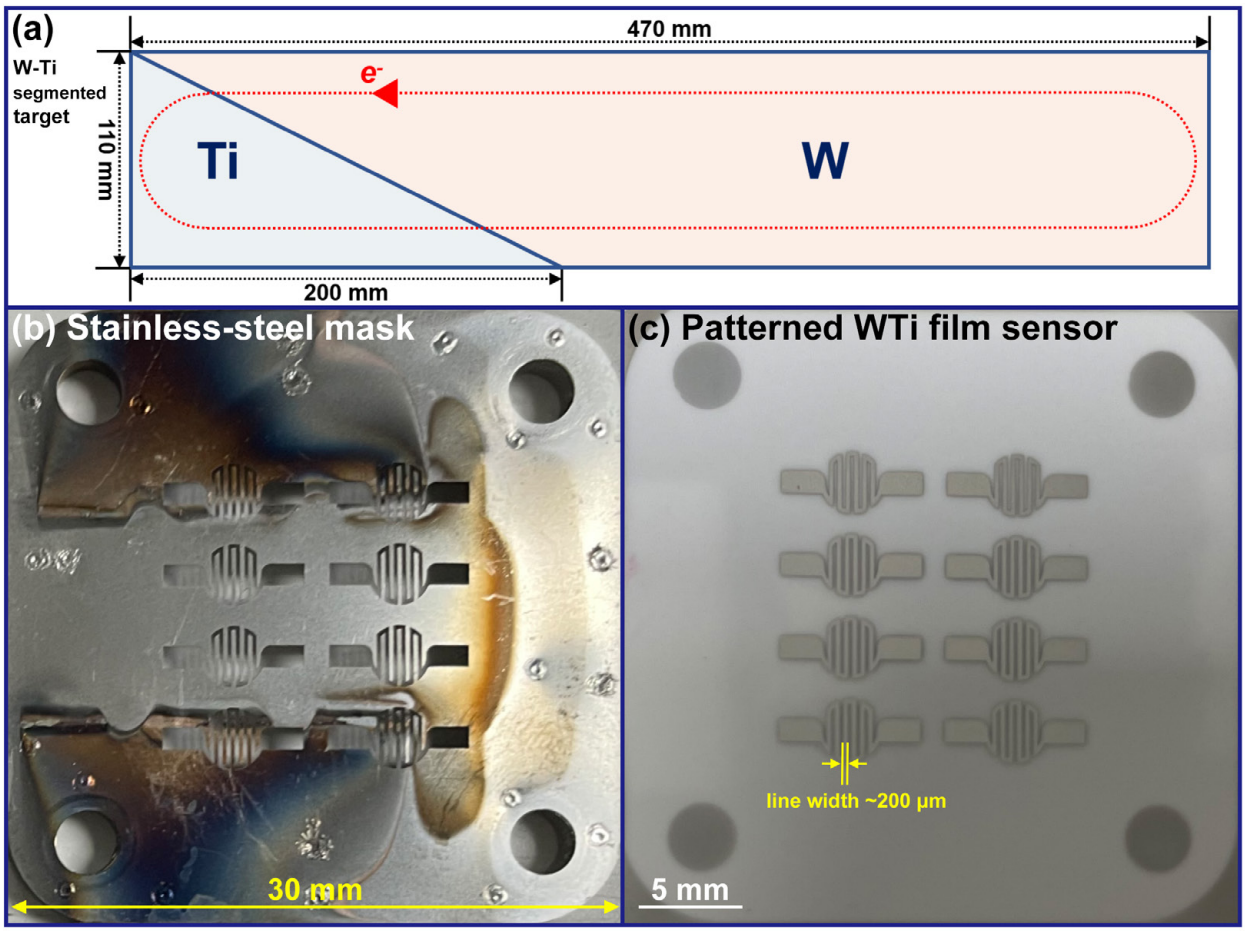

Figure 1. (**a**) Schematic diagram of the W-Ti segmented target, (**b**) image of the stainless-steel mask using for the WTi film deposition, and (**c**) image of the patterned WTi alloy film sensor.

Table 2. Parameters of deposition for the W and WTi films.

Samples	T1	T2	T3	T4	T5	T6
Bias voltage [V]			−100			
Deposition temperature [°C]			300			
Ar flow [sccm]			100			
Deposition pressure [Pa]			0.4			
Target power [kW]			2.3			
Deposition time [min]			30			
Film thickness [nm]	613	591	664	656	624	631
Ti concentrations in WTi [at.%]	0	3.4	6.8	9.6	12.9	22.7

Using scanning electron microscopy (SEM, FEI Nova NanoSEM 430, Hillsboro, OR, USA), the surface and cross-section morphologies of the W and WTi thin film were observed. The phase structure and crystallinity of the films were analyzed by X-ray diffraction (XRD, Bruker D8 advanced, Bruker, MA, USA). An AFM was used to characterize the surface morphology and roughness of the thin films. The TCR value was calculated using the formula TCR = $\Delta R/(R_0 \cdot \Delta T)$, where R_0 is the resistance at temperature 0 °C and TCR is the temperature coefficient of the resistance. During the measurements, an ice-water (deionized water) mixture condition was used to measure the R_0. The sample was heated by a vacuum heating system, and the resistance was measured with a resistance tester to calculate the TCR. For the chamber temperature was measured by using a commercial Pt1000 thermal resistor (class A accuracy, TCR 3.851×10^{-3} K^{-1}). The influence of Ti content on the thermal resistance of Ti-W alloy thin film was studied by changing the content of Ti in the WTi alloy thin film by fixing other technological parameters.

3. Results and Discussion

According to the theory of the conductive mechanism of films, the resistance of films is divided into the resistance within the grain and the resistance at the grain boundary. The increase in the resistance inside the grain increases the TCR, while the increase in the resistance at the grain boundary decreases the TCR. By adding a small number of other metal elements into W, a single-phase solid solution alloy film can be obtained, which can greatly improve the internal resistance of the grain and thus improve the thermal resistance of the film. A small number of Ti atoms in W was added to form a single-phase replacement solid solution, which can improve the thermal resistance of W film. By changing the clamping position of the matrix, WTi alloy films with Ti atomic ratios of 3.4 at.%, 6.8 at.%, 9.6 at.%, 12.9 at.%, and 22.7 at.% were obtained, which were compared with pure W films.

The phase structures of W and WTi alloy thin films were characterized, as shown in Figure 2. The prepared pure W thin film was single-phase α-W with (110) grain orientation (JCPDS No.040806). There were only (110) and (220) characteristic diffraction peaks of α-W in the WTi alloy films with different Ti contents, but no characteristic peaks of Ti, which indicates that there is no elemental Ti in the alloy films, and Ti is all solid dissolved in the W lattice to form a single-phase solid solution. With the increase in the Ti content in the alloy film, the more Ti in the solid solution in the W lattice, the more serious the lattice distortion. The atomic radius of W is 1.41 Å, and the atomic radius of Ti is 1.45 Å. Ti is dissolved using a solution in the lattice of W. Replacing the W atom increased the lattice constant, and the diffraction peak of (110) shifted to a low angle. However, the Ti is soft and a further addition of Ti (9.6~22.7 at.%) reduces the residual stress of the WTi films. With the increase in the Ti content, the full width at half maximum (FWHM) of the (110) diffraction peak increased obviously, and the grain size of the alloy thin film decreased. The average grain sizes of the films were estimated by Debye–Scherrer formula, using the FWHM value of the (110) XRD diffraction peaks. The calculated grain sizes of the WTi films with respect to the Ti content are presented in Table 3. It can be seen that the grain size decreases from 69.4 ± 1.2 nm down to 28.2 ± 1.9 nm with increasing Ti content from 0

to 22.7 at.%. Higher Ti concentrations mean more nucleation sites are provided and result in grain size refinement.

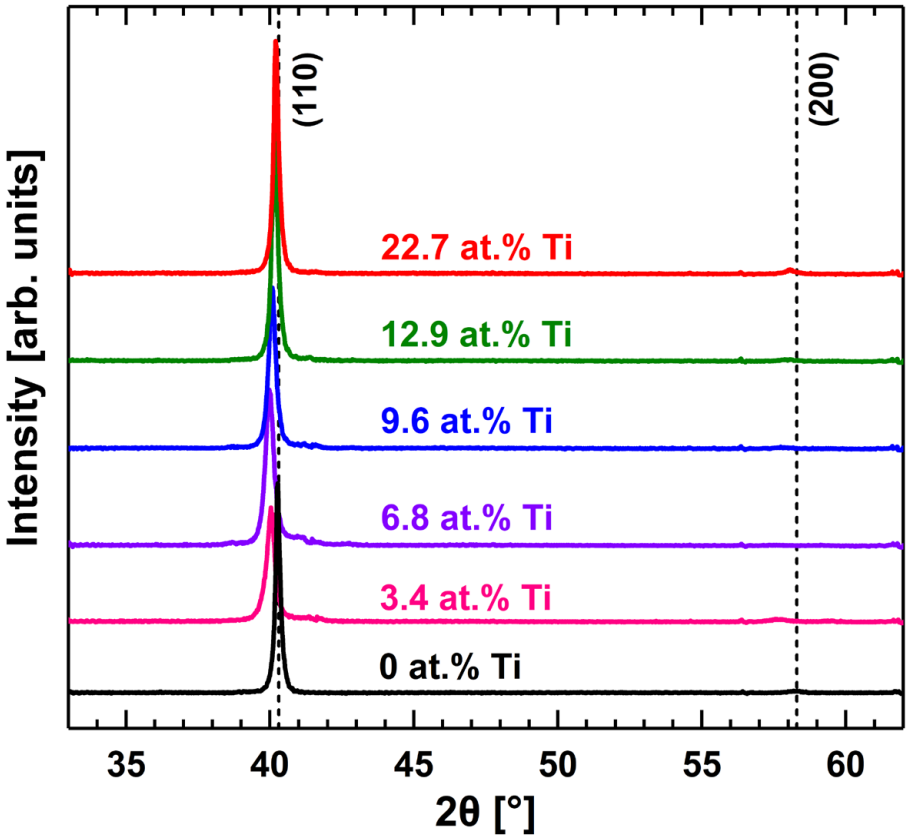

Figure 2. XRD patterns of WTi alloy films as a function of Ti concentrations.

Table 3. Grain sizes of the WTi films with respect to the Ti content.

Concentration of Ti [at.%]	0	3.4	6.8	9.6	12.9	22.7
Grain sizes [nm]	69.4 ± 1.2	56.8 ± 1.4	50.4 ± 1.6	34.1 ± 2.2	29.5 ± 1.1	28.2 ± 1.9

Figure 3 shows the surface section topography of the W and WTi alloy thin films. The surface of both W and WTi films shows an obvious geometric cone shape, clear grain boundaries, and regular stacking, and is compact. The intersections show a dense columnar crystal structure. Compared with the WTi alloy films, the grain size of pure W films is much larger, indicating that the addition of Ti hinders the growth of W grains. The grain boundary of the alloy film is clear, the columnar crystal is obvious, and there is no other structural grain, which indicates that all Ti is solidly dissolved in W, and the single-phase solid solution of WTi alloy is obtained, which is also consistent with the results of XRD.

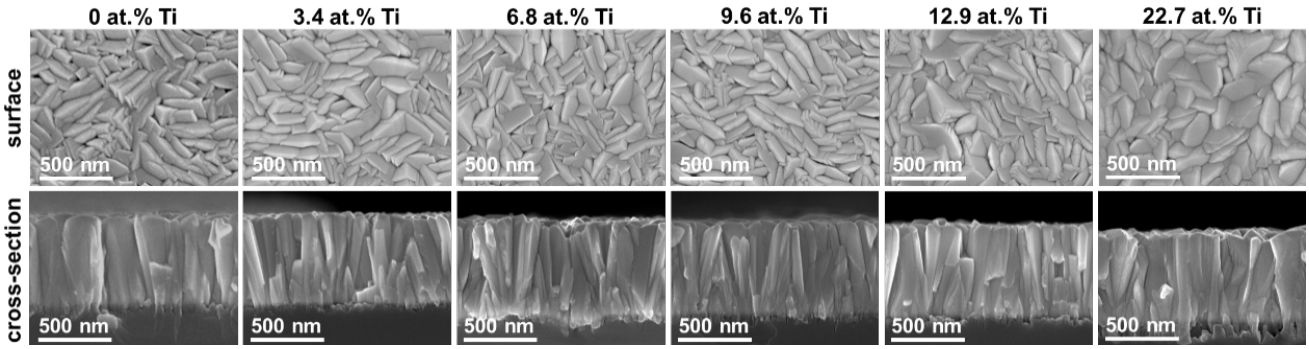

Figure 3. Surface and cross-section SEM images of the WTi alloys films as a function of Ti concentrations.

Due to the small thickness of the film sample, the resistance caused by the scattering of electrons on the film surface accounts for a large proportion of the total resistance, that is, the roughness of the film surface will affect the resistivity of the film. To study the surface roughness of the W and WTi alloy films, an AFM was used to characterize the surface roughness of the samples, as shown in Figure 4. The surface roughness of the pure W film was 14.8 nm. After Ti was added, the surface roughness of the WTi alloy film decreased. This is because the melting point of Ti is smaller than that of W, the undercooling degree of Ti is smaller in the sputtering process, and the diffusion ability is stronger. The roughness of the WTi alloy films with different Ti contents was about 10 nm, and the electron scattering ability of the film surface was similar.

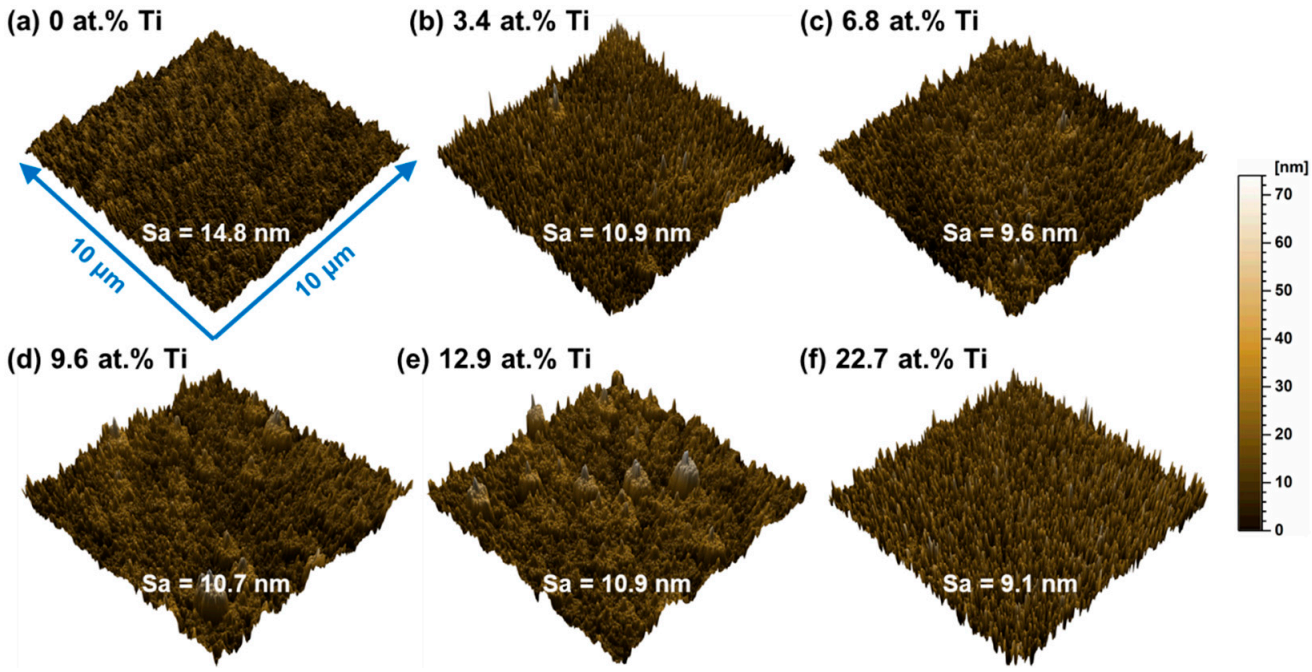

Figure 4. Surface AFM images and roughness of the WTi alloys films as a function of Ti concentrations.

The resistivity of pure W film was 13.3 μΩ·cm, which increased rapidly to 25.9 μΩ·cm (3 at.% Ti) with the increase in Ti content. The highest resistivity was 33.5 μΩ·cm when Ti content was 22.7 at.%, as shown in Figure 5a. After Ti was dissolved in W, some W atoms were replaced, and lattice distortion occurred, the lattice vibration increased, the scattering effect of the lattice on electrons increased, and the resistivity increased. Figure 5b shows the thermal resistance curves of the W and WTi films. The resistance of W and WTi alloy films increased with the increase in temperature, indicating that W and WTi alloys

have positive temperature coefficients. The TCR of pure W films was 5.4 × 10^{-4} K^{-1}, and the TCR increased rapidly to 14.2 × 10^{-4} K^{-1} with the addition of a small amount of Ti. The resistance inside the grain was increased by the Ti replacement of part of W in the W lattice, which made the TCR increase. With the increase in the Ti content, the TCR of the WTi alloy films increased first and then decreased. When Ti content increased from 3.4 at.% to 6.8 at.%, the number of Ti atoms in the solid solution of the W lattice increased, which made the resistance inside the grain increase, the electron scattering ability of the lattice is enhanced, and the TCR increases. As the content of Ti continued to increase, the number of Ti atoms in solid solution further increased, and the TCR of Ti was less than that of W (TCR_W = 0.0049/K, TCR_{Ti} = 0.0041/K), which made the TCR of the alloy thin film decrease. Moreover, with the increase in Ti content, the grain size of the WTi alloy film decreased, which also led to a decrease in TCR. When Ti content was 6.8 at.%, TCR reached the maximum value of 19.5 × 10^{-4} K^{-1}. Compared with the pure W films, TCR increased by 3.6 times, and the linearity of linear fitting was very high, indicating that the WTi alloy films have good thermal resistance.

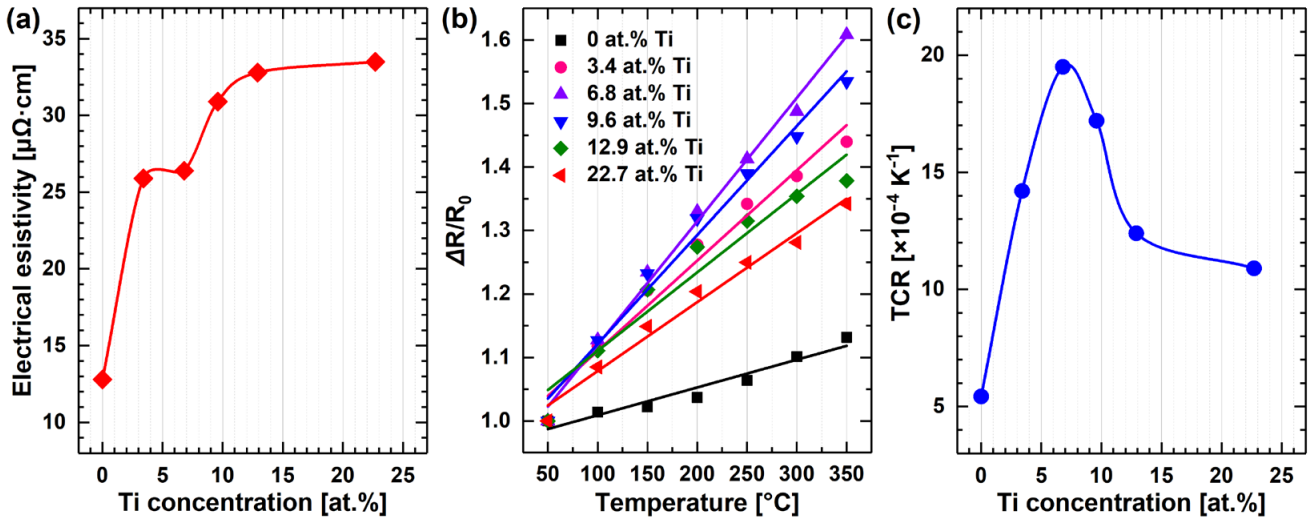

Figure 5. (**a**) Room-temperature electrical resistivity, (**b**) thermal resistance curves, and (**c**) TCR values of the WTi alloy films as a function of Ti concentrations.

The thermal resistance repeatability test was carried out for the WTi film with 6.8 at.% Ti content. Figure 6 shows the (a) thermal resistance curve and (b)TCR of the 6.8 at.% Ti alloy film after repeated tests. After being repeated at different times, the resistance of the WTi film increased with the increase in temperature, but the slope of the thermal resistance curve decreased gradually, the increase in resistance decreased, and the TCR decreased gradually. Figure 7 shows the microstructure of the alloy film in the deposition state and after one and five repetitions. After the thermal resistance test, the surface of the WTi alloy film was a still flattened strip structure, and the cross-section had a compact columnar crystal structure. With the increase in the number of repetitions and the longer the total time of the WTi alloy film at a high temperature, part of the internal stress was released, a few holes appeared, and the film densification decreased. In order to further understand the change in the microstructure of the WTi alloy film at a high temperature and the reason for the TCR decrease, we conducted the annealing treatment of the alloy film.

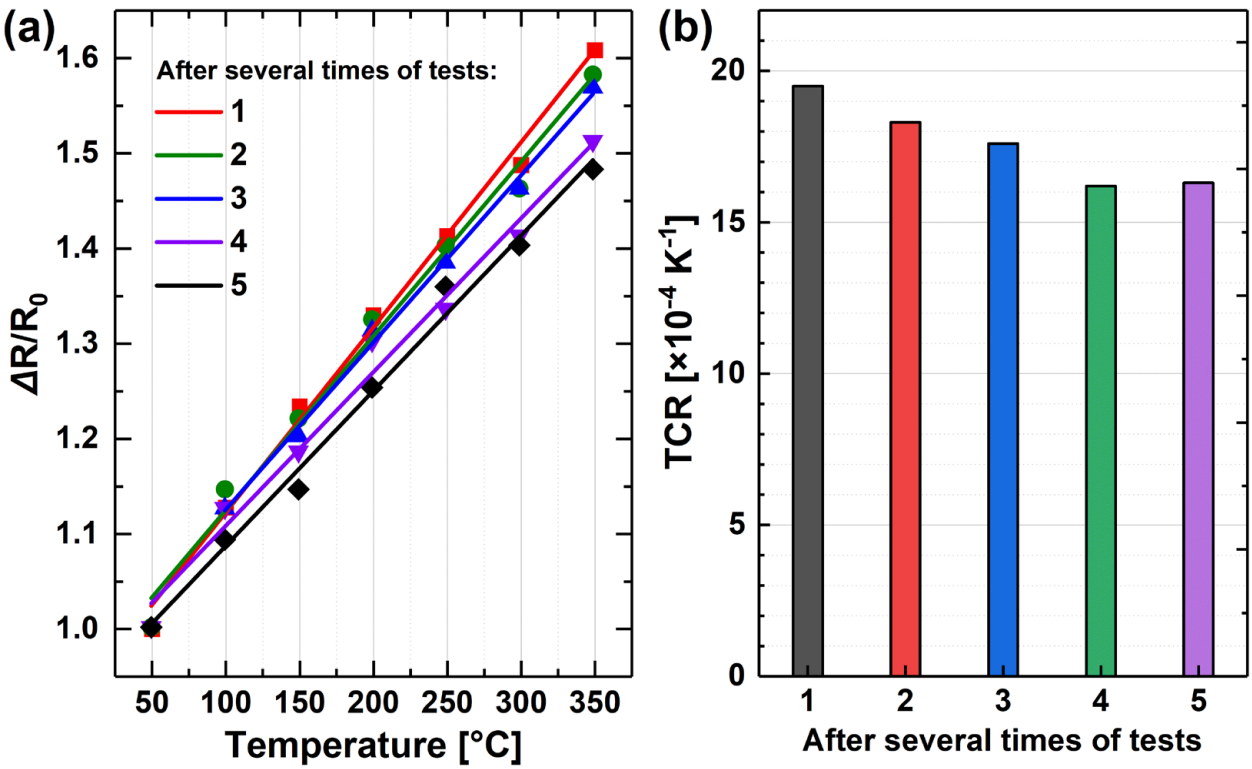

Figure 6. (**a**) Thermal resistance curves and (**b**) TCR values of the WTi alloy film with 6.8 at.% Ti after cycled thermal resistance measurements.

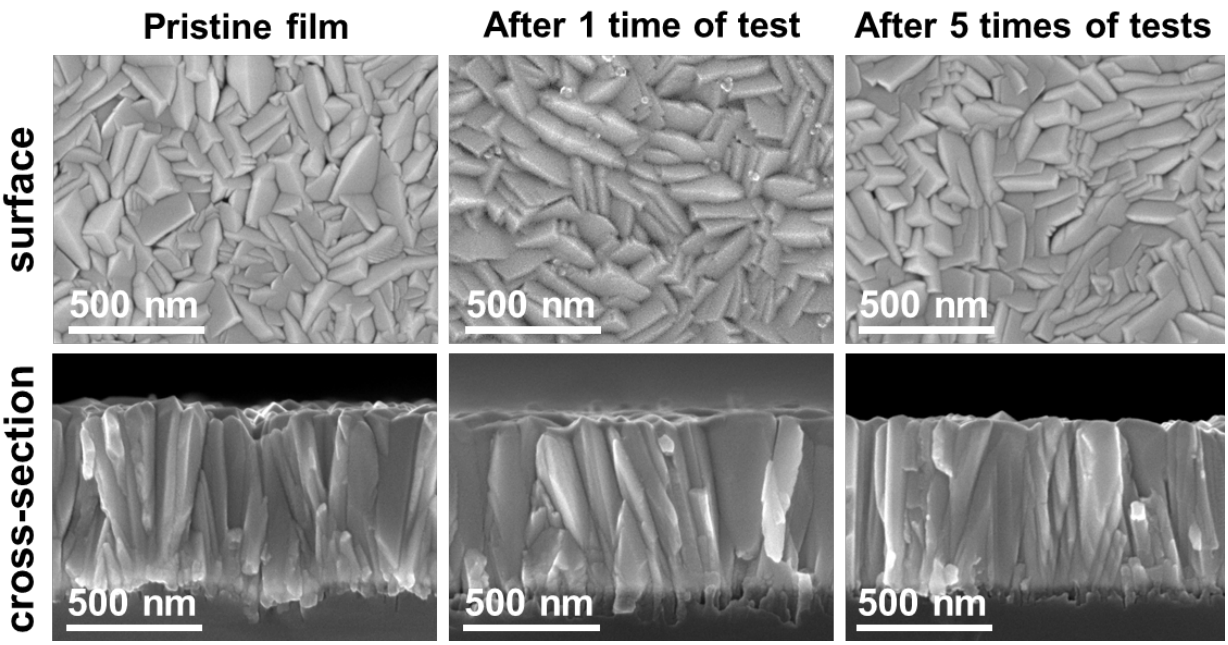

Figure 7. Surface and cross-section SEM images of the WTi alloy film with 6.8 at.% Ti after cycled-thermal-resistance measurements.

The phase structure of the annealed WTi alloy with a Ti content of 6.8 at.% was characterized by XRD, as shown in Figure 8. A partially enlarged view is shown on the right side. The annealed XRD has only the characteristic diffraction peak of α-W, but no characteristic peak of Ti, which indicates that the annealed alloy film still has a single-phase solid solution structure, and all Ti is dissolved in a solution in the W lattice. After annealing, the half-height width of the (110) diffraction peak increased and the grain was refined. As can be seen from the locally enlarged image on the right of Figure 8, the diffraction peak of (110) shifts to a high angle after annealing, and the compressive stress generated in the deposition process of the film is released.

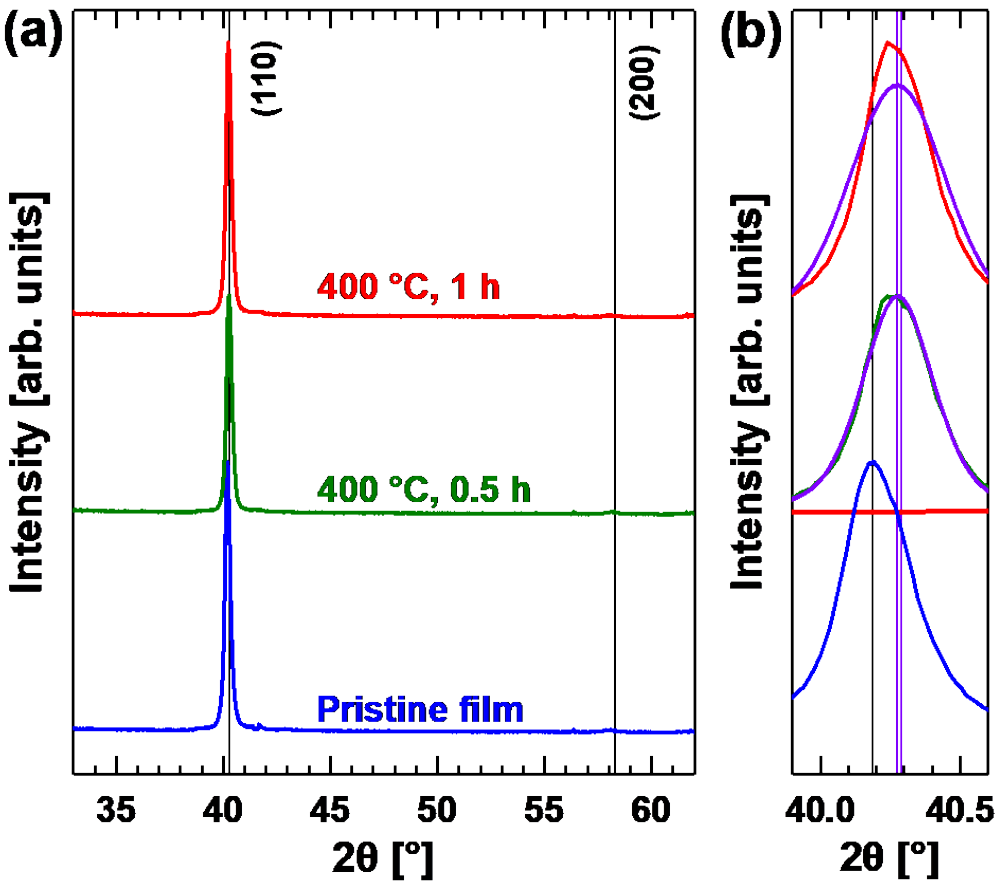

Figure 8. (**a**) XRD patterns of the WTi alloy film with 6.8 at.% Ti after vacuum annealing at 400 °C for 0~1 h and (**b**) expanded-scale XRD patterns around the W (110).

The microstructure of the WTi alloy films before and after annealing and at different annealing times is shown in Figure 9. After annealing, the surface and cross-section of the alloy film do not change considerably: the surface has a leveled strip structure and the cross-section has a columnar crystal structure. After annealing, the grain size of the WTi alloy film increased, a few pores appeared, and the density of the film decreased. When the annealing time increased from 30 min to 60 min, the grain size further increased and the density of the alloy film further decreased. There is compressive stress in the deposited WTi alloy film, which makes the structure of the film denser and the width of the grain boundary smaller. The surface roughness of the WTi alloy film after annealing is shown in Figure 10. The surface roughness of the WTi alloy film before and after annealing was about 9 nm, and the electron scattering ability of the film surface does not change.

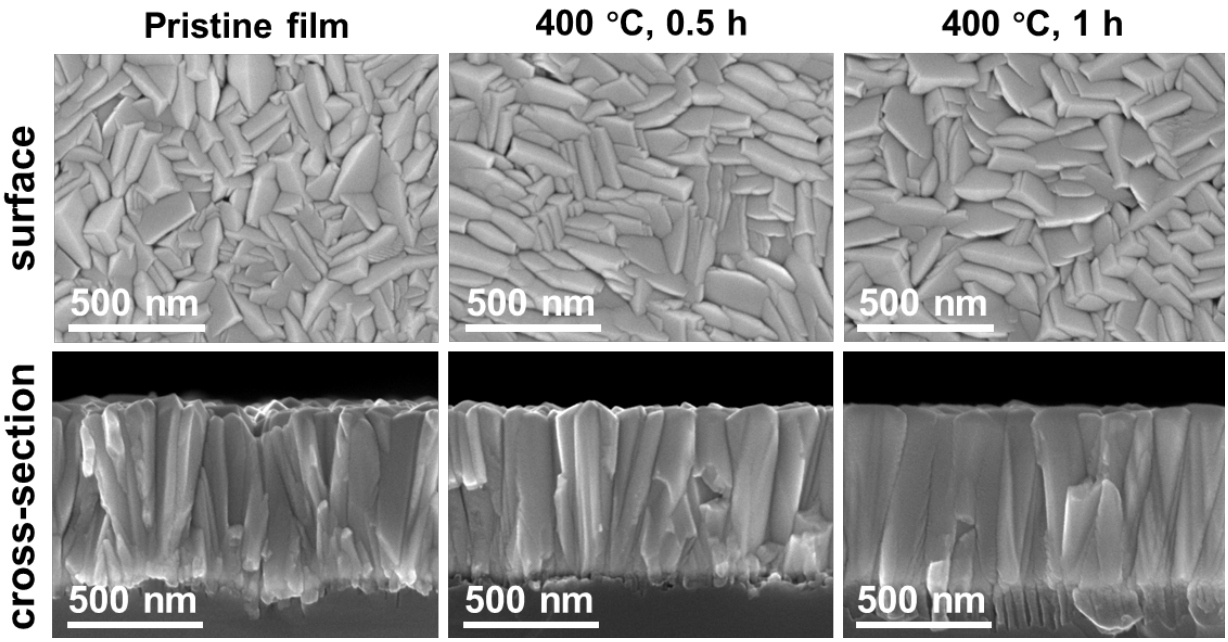

Figure 9. Surface and cross-section SEM images of the WTi alloy film with 6.8 at.% Ti after vacuum annealing at 400 °C for 0~1 h.

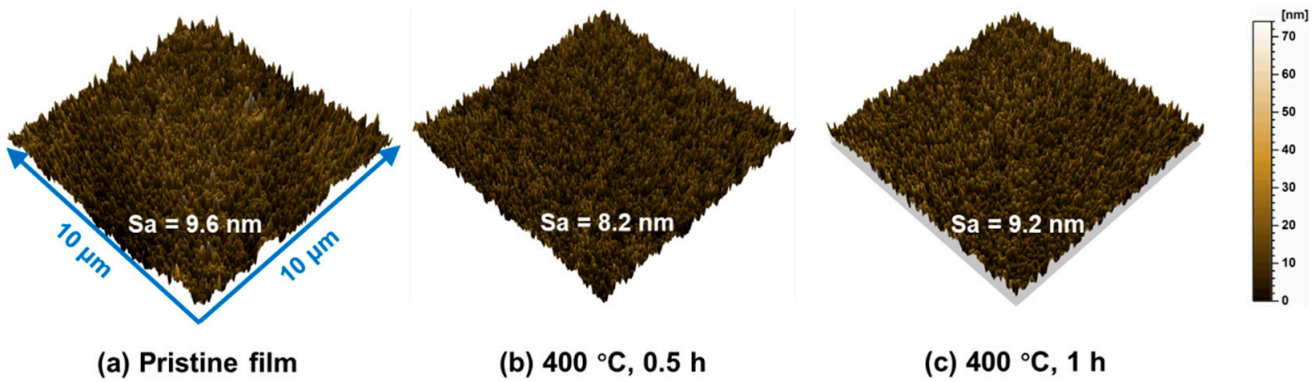

Figure 10. Surface AFM images and roughness of the WTi alloy film with 6.8 at.% Ti after vacuum annealing at 400 °C for 0~1 h.

The structure of the deposited WTi films is denser, the scattering effect of grain boundary on the electron is lower, and the resistivity is lower. After annealing, the density of the alloy film decreased and holes appeared, which increases the resistivity of the film, as shown in Figure 11a. Figure 11b shows the thermal resistance curves of the 6.8 at.% Ti alloy films annealed at different times. When the annealing time increased from 30 min to 60 min, the thermal resistance curves basically coincided and the TCR remained unchanged, indicating that the structure and thermal resistance of the WTi alloy films reach a stable state after annealing for 30 min. After annealing for 30 min, the TCR of 6.8 at.% Ti alloy film was 14×10^{-4} K^{-1}, and the linearity of the linear fitting was high, which indicates that the WTi alloy film has a good thermal resistance after annealing for 30 min.

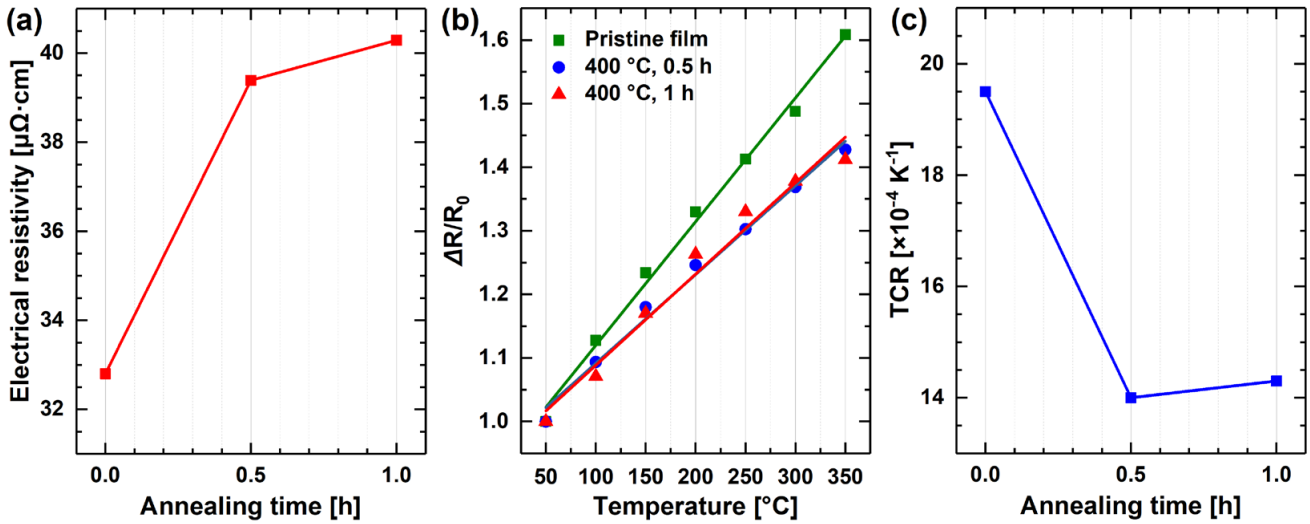

Figure 11. (**a**) Room-temperature electrical resistivity, (**b**) thermal resistance curves, and (**c**) TCR values of the WTi alloy film with 6.8 at.% Ti as a function of vacuum-annealing time.

The repeatability of the 6.8 at.% Ti alloy film after annealing for 30 min was characterized, as shown in Figure 12. After annealing, the thermal resistance of the alloy film tends to be stable several times. Except for the first time, the thermal resistance curves of the other four times basically coincided, and the TCR also tended to be stable. The results show that, after annealing for 30 min, the structure of the 6.8 at.% Ti alloy film does not change and the thermal resistance remains stable.

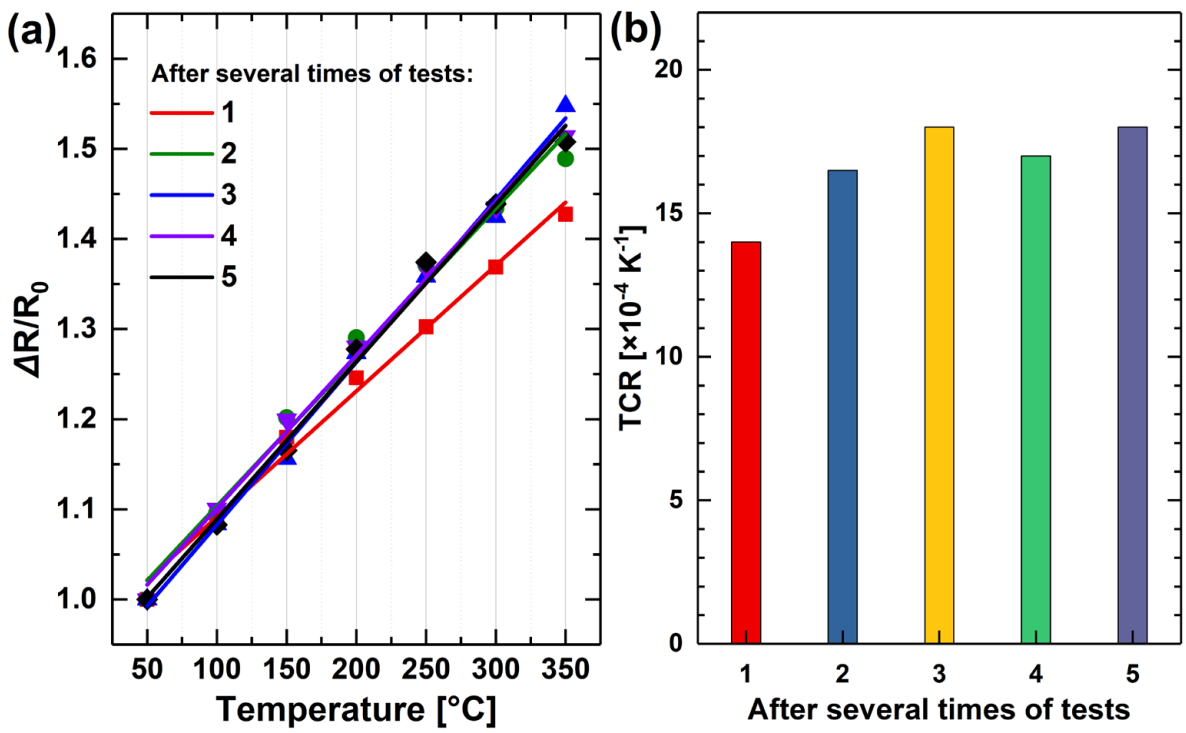

Figure 12. (**a**) Thermal-resistance curves, (**b**) TCR values of annealed WTi alloy film with 6.8 at.% Ti after cycled-thermal-resistance measurements.

4. Conclusions

In this paper, WTi alloy thin films with Ti concentrations up to 22.7 at.% were prepared. The effects of varying Ti concentration on the microstructure and thermal resistance of the WTi alloy films were studied. The effect and mechanism of the annealing treatment on the structure, measurement accuracy, and thermal resistance stability of the WTi alloy films were discussed. The Ti was dissolved in the W lattice to form a single-phase solid solution, showing a columnar structure. When the Ti atomic ratio was increased to 6.8 at.%, the TCR of film reached 19.5×10^{-4} K^{-1}. With the further increase, the Ti content to 22.7 at.%, the TCR decreased to 10.9×10^{-4} K^{-1}. Ti dissolved in a solution in the W lattice increased the vibration of the atoms in the lattice, the scattering of electrons increased, the internal resistance of the grain increased, and the TCR increased.

After multiple thermal resistance tests of the as-deposited films, a small number of pores appeared and the film densification decreased, resulting in the TCR of the alloy film decreasing gradually. After five cycles, the TCR of the alloy film with 6.8 at.% Ti decreased from 19.5 to 16.3×10^{-4} K^{-1}. After annealing at 400 °C for 30 min, the TCR value decreased to 14×10^{-4} K^{-1}. With further increasing the annealing time, the microstructure and thermal resistance properties of the WTi alloy thin film with 6.8 at.% Ti keep stable.

Author Contributions: Conceptualization, Z.W. and Q.W.; methodology, Y.Z.; software, Y.Z.; validation, Z.W., Y.Z. and Q.W.; formal analysis, Y.Z.; investigation, Z.W.; resources, Y.Z.; data curation, Q.W.; writing—original draft preparation, Z.W.; writing—review and editing, K.-H.K. and S.-H.K.; visualization, Z.W.; supervision, Q.W.; project administration, Q.W., K.-H.K. and S.-H.K.; funding acquisition, Q.W. All authors have read and agreed to the published version of the manuscript.

Funding: This research was funded by the National Key Research and Development Project of China (2017YFE0125400) and the National Natural Science Foundation of China (51901048).

Institutional Review Board Statement: Not applicable.

Informed Consent Statement: Not applicable.

Data Availability Statement: Not applicable.

Acknowledgments: The authors gratefully acknowledge the financial support of the National Key Research and Development Project of China (2017YFE0125400) and the National Natural Science Foundation of China (51901048).

Conflicts of Interest: The authors declare no conflict of interest.

References

1. Xiao, C.; Zhao, L.; Asada, T.; Odendaal, W.; Van Wyk, J. An overview of integratable current sensor technologies. In Proceedings of the 38th IAS Annual Meeting on Conference Record of the Industry Applications Conference, Salt Lake City, UT, USA, 12–16 October 2003; Volume 2.
2. Mizuta, M. Temperature Sensor Circuit Having Trimming Function. U.S. Patent 6,674,185, 6 January 2004.
3. Andrejevic, M.; Burdon, M. Defining the Sensor Society. *Telev. New Media* **2014**, *16*, 19–36. [CrossRef]
4. Grattan, V.; Sun, T. Fiber optic sensor technology an overview. *Sens. Actuators A* **2000**, *82*, 40–61. [CrossRef]
5. Calkins Frederick, T.; Flatau Alison, B.; Dapino Marcelo, J. Overview of Magnetostrictive Sensor Technology. *J. Intell. Mater. Syst. Struct.* **2016**, *18*, 1057–1066. [CrossRef]
6. Ramakrishnan, M.; Rajan, G.; Semenova, Y.; Farrell, G. Overview of Fiber Optic Sensor Technologies for Strain/Temperature Sensing Applications in Composite Materials. *Sensors* **2016**, *16*, 99. [CrossRef] [PubMed]
7. Giallorenzi, T.; Bucaro, J.; Dandridge, A.; Sigel, G.; Cole, J.; Rashleigh, S.; Priest, R. Optical Fiber Sensor Technology. *IEEE Trans. Microw. Theory Tech.* **1982**, *30*, 472–511. [CrossRef]
8. Mattmann, C.; Clemens, F.; Tröster, G. Sensor for Measuring Strain in Textile. *Sensors* **2008**, *8*, 3719–3732. [CrossRef]
9. Zhang, J.; Nagao, Y.; Kuwano, S.; Ito, Y. Microstructure and Temperature Coefficient of Resistance of Platinum Films. *JPN J. Appl. Phys.* **1997**, *36*, 834–839. [CrossRef]
10. Schmidl, G.; Dellith, J.; Kessler, E.; Schinkel, U. The influence of deposition parameters on Ti/Pt film growth by confocal sputtering and the temperature dependent resistance behavior using SiOx and Al2O3 substrates. *Appl. Surf. Sci.* **2014**, *313*, 267–275. [CrossRef]

11. Shaun, F.J.; Nefzaoui, E.; Hossain, N.; Marty, F.; Bourouina, T. Thin-Film Thermoresistive Platinum Sensor for Water Temperature Measurement. In Proceedings of the 2019 IEEE International Conference on Power, Electrical and Electronics and Industrial Applications (PEEIACON), Dhaka, Bangladesh, 29 November–1 December 2019; pp. 57–60. [CrossRef]
12. Wada, M.; Maeda, T.; Inoue, S. Single Crystal Level High Temperature Coefficient of Resistance for a Platinum Thin Film on a Sapphire Substrate by Thermal Treatment. *J. JPN Inst. Met. Mater.* **2012**, *76*, 359–363. [CrossRef]
13. Yan, W.; Li, H.; Liu, J.; Guo, J. EPMA and XRD study on nickel metal thin film for temperature sensor. *Sens. Actuators A Phys.* **2007**, *136*, 212–215. [CrossRef]
14. Turkani, V.; Maddipatla, D.; Narakathu, B.; Altay, B.; Fleming, D.; Bazuin, B.; Atashbar, M. A screen-printed nickel based resistance temperature detector (RTD) on thin ceramic substrate. In Proceedings of the 2020 IEEE International Conference on Electro Information Technology (EIT), Chicago, IL, USA, 31 July–1 August 2020; pp. 577–580. [CrossRef]
15. Cui, J.; Liu, H.; Li, X.; Jiang, S.; Zhang, B.; Song, Y.; Zhang, W. Fabrication and characterization of nickel thin film as resistance temperature detector. *Vacuum* **2020**, *176*, 109288. [CrossRef]
16. Sun, B.; Wang, P.; Ma, B.; Deng, J.; Luo, J. Effects of annealing on the temperature coefficient of resistance of nickel film deposited on polyimide substrate. *Vacuum* **2018**, *160*, 18–24. [CrossRef]
17. Xidong, L. *Preparation of Thermistor Sensing Film by Arc Ion Plating*; Northeastern University: Boston, MA, USA, 2004.
18. Stankevi, V.; Slmkevlcms, C. Application of aluminum films as temperature sensors for the compensation of output thermal shift of silicon piezoresistive pressure sensors. *Sens. Actuators A* **1998**, *71*, 161–166. [CrossRef]
19. Oliva, A.I.; Lugo, J.M. Measurement of the Temperature Coefficient of Resistance in Metallic Films with Nano-thickness. *Int. J. Thermophys.* **2016**, *37*, 35. [CrossRef]
20. Xiaoping, W. Effect of grain size on temperature coefficient of film resistivity. *J. Phys.* **1994**, *195*, 214–220.
21. Eom, T.H.; Han, J.I. The effect of the nickel and chromium concentration ratio on the temperature coefficient of the resistance of a Ni–Cr thin film-based temperature sensor. *Sens. Actuators A Phys.* **2017**, *260*, 198–205. [CrossRef]
22. Jian, Z. *Preparation and Performance of Nanometer Thin Film Temperature Sensor*; Northeastern University: Boston, MA, USA, 2007.
23. Weihong, M.; Changlong, C. Effect of magnetron sputtering parameters on temperature characteristics of film resistance of titanium-tungsten alloy. *Surf. Technol.* **2011**, *40*, 85–87.
24. Mizoshiri, M.; Ito, Y.; Arakane, S.; Sakurai, J.; Hata, S. Direct fabrication of Cu/Cu_2O composite micro-temperature sensor using femtosecond laser reduction patterning. *JPN J. Appl. Phys.* **2016**, *55*, 06GP05. [CrossRef]
25. Sungpill, N.; Hyunji, N.; Sunggap, L. Electrical properties of vanadium tungsten oxide thin films. *Mater. Res. Bull.* **2010**, *45*, 291–294.
26. Cacucci, A.; Potin, V.; Imhoff, L.; Martin, N. Structural and electrical properties in tungsten/tungsten oxide multilayers. *Thin Solid Films* **2013**, *553*, 93–97. [CrossRef]
27. Wang, Y.; Zhang, C.; Li, J.; Ding, G.; Duan, L. Fabrication and characterization of ITO thin film resistance temperature detector. *Vacuum* **2016**, *140*, 121–125. [CrossRef]
28. Sundeen, J.; Buchanan, R. Thermal sensor properties of cermet resistor films on silicon substrates. *Sens. Actuators A Phys.* **2001**, *90*, 118–124. [CrossRef]
29. Mehmood, Z.; Mansoor, M.; Haneef, I.; Ali, S.Z.; Udrea, F. Evaluation of thin film p-type single crystal silicon for use as a CMOS Resistance Temperature Detector (RTD). *Sens. Actuators A Phys.* **2018**, *283*, 159–168. [CrossRef]
30. Sarma, S.; Lee, J.H. Developing Efficient Thin Film Temperature Sensors Utilizing Layered Carbon Nanotube Films. *Sensors* **2018**, *18*, 3182. [CrossRef]
31. Lee, E.-B.; Hwang, I.-S.; Cha, J.-H.; Lee, H.-J.; Lee, W.-B.; Pak, J.J.; Lee, J.-H.; Ju, B.-K. Micromachined catalytic combustible hydrogen gas sensor. *Sens. Actuators B Chem.* **2011**, *153*, 392–397. [CrossRef]
32. Lv, W.; Wang, Y.; Shi, W.; Cheng, W.; Huang, R.; Zhong, R.; Zeng, Z.; Fan, Y.; Zhang, B. Role of micro-nano fabrication process on the temperature coefficient of resistance of platinum thin films resistance temperature detector. *Mater. Lett.* **2021**, *309*, 131313. [CrossRef]
33. Weng, S.; Qiao, L.; Wang, P. Thermal stability of Pt-Ti bilayer films annealing in vacuum and ambient atmosphere. *Appl. Surf. Sci.* **2018**, *444*, 721–728. [CrossRef]
34. Schössler, T.; Schön, F.; Lemier, C.; Urban, G. Effect of high temperature annealing on resistivity and temperature coefficient of resistance of sputtered platinum thin films of SiO2/Pt/SiOx interfaces. *Thin Solid Films* **2020**, *698*, 137877. [CrossRef]
35. Lin, X.; Zhang, C.; Yang, S.; Guo, W.; Zhang, Y.; Yang, Z.; Ding, G. The impact of thermal annealing on the temperature dependent resistance behavior of Pt thin films sputtered on Si and Al_2O_3 substrates. *Thin Solid Films* **2019**, *685*, 372–378. [CrossRef]
36. Kim, N.H.; Na, D.M.; Ko, P.J.; Park, J.S.; Lee, W.S. Electrical and Thermal Properties of Platinum Thin Films Prepared by DC Magnetron Sputtering for Micro-Heater of Microsensor Applications after CMP Process. *Solid State Phenom.* **2007**, *124–126*, 267–270. [CrossRef]